LANGMUIR

Article

pubs.acs.org/Langmuir

Water-Proton Relaxivities of Radical Nanoparticles Self-Assembled via Hydration or Dehydration Processes

Kosuke Morishita,[†] Yuna Okamoto,[†] Shuhei Murayama,[‡] Kazuteru Usui,[†] Eriko Ohashi,[†] Go Hirai,[†] Ichio Aoki,[‡] and Satoru Karasawa*[,†,§,∥]

[†]Graduate School of Pharmaceutical Sciences, Kyushu University, 3-1-1 Maidashi, Higashi-Ku, Fukuoka 812-8582, Japan

[‡]Department of Molecular Imaging and Theranostics, National Institute of Radiological Sciences (NIRS), Group of Quantum-State Controlled MRI, QST, Anagawa 4-9-1, Inage, Chiba-city 263-8555, Japan

[§]PRESTO, Japan Science and Technology Agency, Kawaguchi 332-0012, Japan

[∥]Showa Pharmaceutical University, 3-3165 Higashi-Tamagawagakuen, Machida 194-8543, Japan

Supporting Information

ABSTRACT: Nanoparticles capable of accumulating in tumor tissues are promising materials for tumor imaging and therapy. In this study, two radical nanoparticles (RNPs), denoted as **1** and **2**, composed of self-assembled ureabenzene derivatives possessing one or two amphiphilic side chains were demonstrated to be candidates for metal-free functional magnetic resonance imaging (MRI) contrast agents (CAs). Because of the self-assembly behavior of **1** and **2** in a saline solution, spherical RNPs of sizes ∼50−90 and ∼30−100 nm were detected. In a highly concentrated solution, **RNP 1** showed considerably small water-proton relaxivity values (r_1 and r_2), whereas **RNP 2** showed an r_1 value that was around 5 times larger than that of **RNP 1**. These distinct r_1 values might be caused by differences in the self-assembly behavior by a hydration or dehydration process. In vivo studies with **RNP 2** demonstrated a slightly enhanced T_1-weighted image in mice, suggesting that the RNPs can potentially be used as metal-free functional MRI CAs for T_1-weighted imaging.

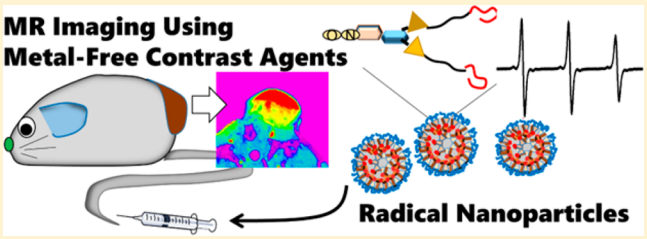

INTRODUCTION

Tumor cells have been found to exhibit higher activity than normal cells, which leads to the formation of disordered morphologies in the tumor tissue.[1,2] Therefore, the tumor tissue possesses void spaces that are approximately 10−500 nm in size.[3,4] Furthermore, intercellular spaces are present around the endothelial cells, which allow effective permeation and retention of nanoparticles (NPs) into the tumor tissue. Utilizing the enhanced permeation and retention (EPR) effect of NPs through these void spaces,[5,6] many drug delivery systems (DDSs) and tumor imaging agents are being developed.

In the case of bioimaging using magnetic resonance imaging (MRI), NPs of Gd complexes have been studied and are currently being used as tumor imaging contrast agents (CAs).[7,8] However, potential side effects such as renal disorders and accumulation in the brain pose challenges.[9,10] On the other hand, CAs consisting of organic radicals are being paid wide attention as metal-free MRI CAs, which are expected to have fewer side effects than metal ion-based CAs.[11,12]

We have been studying the self-assembly behavior of ureabenzene derivatives (**UBD**s) with amphiphilic side chains that are composed of an alkyl group and an oligoethylene glycol (OEG) group (Scheme 1).[13] A **UBD** has multiple functional groups, for instance, urea for hydrogen bonds, benzene for $\pi-\pi$ stacking, alkyl chains as a hydrophobic moiety, and OEG as the hydrophilic group. Therefore, it is readily soluble in water and is capable of self-assembly by the above-mentioned intermolecular interactions. Previously, **UBD** analogue-based stable **TEMDO** (2,2,6,6-tetramethyl-3,6-dihydropyridin-1-oxyl) or **TEMPO** (2,2,6,6-tetramethylpiperidin-1-oxyl) units incorporated in a benzene ring or in the tertiary amine in a side chain, **TEMDO-UBD** and **TEMPO-UBD**, were synthesized as candidates for metal-free CAs (Scheme 1).[14] Both derivatives formed radical nanoparticles (RNPs) by self-assembly in aqueous solutions and were characterized by higher relaxivity values (r_1 and r_2) than those of TEMPO radicals of smaller sizes. Suppression of the molecular motion (tumbling) due to the formation of the RNPs effectively increases the rotational correlation time (τ_R),[15,16] resulting in higher relaxivity values. The higher relaxivity values of the RNPs make it possible to use them as MRI CAs as they yield enhanced T_1- and T_2-weighted images. Thus, taking advantage of the RNPs is of great significance not only for targeting tumor accumulation but also for tumor imaging using MRI. However, both **TEMDO-UBD** and **TEMPO-UBD** have multiple OEGs (e.g., four or three

Received: April 3, 2017
Revised: June 28, 2017
Published: July 5, 2017

DOI: 10.1021/acs.langmuir.7b01126
Langmuir 2017, 33, 7810−7817

Scheme 1. Molecular Structures of UBD, TEMPO-UBD, TEMDO-UBD, 1 (TEMDO-UBD-MA), and 2(TEMDO-UBD-DA)

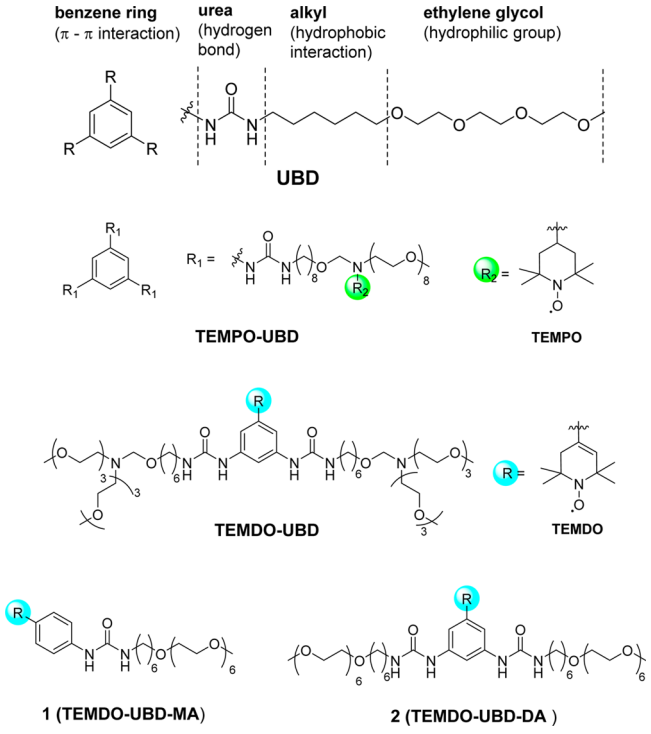

OEGs in a molecule) that are highly hydrophilic, resulting in RNPs of lower concentrations and a high critical aggregation concentration (CAC). Therefore, both derivatives face a problem in which the relaxivity values of the RNPs at low concentration exhibit smaller values than those in highly concentrated solutions. In this study, we demonstrated the construction of **TEMDO-UBD** by introducing one or two amphiphilic side chains into a benzene ring, and these are denoted as **1** (**TEMDO-UBD-MA**) and **2** (**TEMDO-UBD-DA**) (Figure 1). Thus, **1** and **2** that have one or two OEG

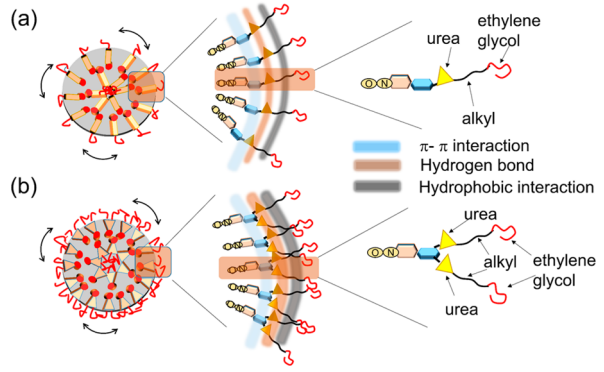

Figure 1. Illustrations of plausible structures of RNP **1** (a) and **2** (b) with multiple binding sites.

groups are predicted to readily form RNPs with smaller CAC values and exhibit higher relaxivity values at the same time. Herein, we describe the self-assembly behavior and the variation in the relaxivity values of **RNPs 1** and **2**, accompanied by in vivo MRI examination.

EXPERIMENTAL SECTION

General Information. Infrared and UV−vis spectra were recorded on a JASCO 420 FT-IR spectrometer and a JASCO V570 spectrometer, respectively. ^{1}H nuclear magnetic resonance (NMR) spectra were recorded on a Bruker Biospin AVANCE III 500 Fourier transform spectrometer using $CDCl_3$ or DMSO-d_6 or D_2O using TMS as the standard. High-resolution mass spectra (HRMS) using electrospray ionization (ESI) mass spectra (ESI-MS) were recorded on a Bruker Daltonics microTOF spectrometer. Electron spin resonance (ESR) spectra were recorded on a Bruker Biospin ESR300 EPR X-band (9.4 GHz) spectrometer equipped with a microwave frequency counter. Sample solutions in saline were placed in capillary tubes and were measured at 25 °C. Dynamic light scattering (DLS) measurements were performed on a Zetasizer Nano ZS (Malvern Instruments Ltd.).

Materials. Unless otherwise stated, all reagents and solvents were used as received without further purification. 2,5,8,11,14,17,20-Heptaoxahexacoscan-26-amine ($Eg_6C_6NH_2$) and tetramethyl-4-(4,4,5,5-tetramethyl-1,3,2-dioxaborolan-2-yl)-3,6-dihydropyridin-1(2*H*)-yloxyl radicals were prepared according to previous reports.[7] Thin-layer chromatography (TLC) was performed on silica gel plates 60 F_{254} (Merck).

*1-(2,5,8,11,14,17,20-Heptaoxahexacosan-26-yl)-3-(4-iodophenyl)urea (**Iodo-UBD-MA**).* A solution of 4-iodobenzoic acid (496 mg, 2 mmol) in $SOCl_2$ (30 mL) was refluxed for 2 h and evaporated under reduced pressure to produce crude 4-iodobenzoyl chloride. To a solution of the crude mixture in THF (4 mL), an aqueous solution of NaN_3 (429 mg, 6.6 mmol) was added, and the solution mixture was stirred in an ice bath for 2 h. Saturated $NaHCO_3$ solution was added to the reaction flask at the end of 2 h and extracted with toluene three times. The combined organic layer was dried over $MgSO_4$ and evaporated under reduced pressure until the remaining volume was 15 mL; the resultant product is a toluene solution of 4-iodoisophthaloyl azide. Without purification, the crude reaction mixture was refluxed for 2 h to produce a toluene solution of 1-iodo-4-isocyanatobenzene. To a solution of 1-iodo-4-benzoyl azide in toluene, $Eg_6C_6NH_2$ (870 mg, 2.2 mmol) in 4 mL of $CHCl_3$ was added dropwise and stirred overnight in an ice bath at room temperature. The reaction mixture was evaporated under reduced pressure, and the crude residue was chromatographed on silica gel using $CHCl_3$/MeOH solution (100:1−50:1) as the eluent to obtain a yellowish oil (1.02 g, 1.60 mmol, 80%). IR (NaCl, cm^{-1}) 3491, 3340, 2930, 2864, 1695, 1594, 1538, 1449, 1351, 1305, 1261, 1201, 1111, 1028. ^{1}H NMR (DMSO-d_6, 500 MHz) δ 8.49 (*s*, 1H), 7.51 (*d*, *J* = 9.0 Hz, 2H), 7.23 (*d*, *J* = 9.0 Hz, 2H), 6.14 (*t*, *J* = 5.5 Hz, 1H), 3.51−3.41 (*m*, 26H), 3.24 (*s*, 3H), 3.05 (*q*, *J* = 6.5 Hz, 4H), 1.49 (*quin*, *J* = 6.8 Hz, 2H), 1.41 (*quin*, *J* = 6.8 Hz, 4H), 1.33−1.26 (*m*, 4H). ^{13}C NMR ($CDCl_3$, 126 MHz) δ 155.79, 140.06, 137.78, 120.73, 84.36, 71.97, 71.10, 70.88, 70.70, 70.66, 70.12, 59.11, 39.78, 29.62, 29.09, 26.15, 25.77. ESI-MS *m*/*z* 663.21 $[M + Na]^+$. HRMS (ESI-TOF) calculated for $C_{26}H_{45}N_2O_8INa$ $[M + Na]^+$, 663.2113; found, 663.2127.

*1,1′-(5-Iodo-1,3-phenylene)bis(3-(2,5,8,11,14,17,20-heptaoxahexacosan-26-yl)urea) (**Iodo-UBD-DA**).* **Iodo-UBD-DA** was prepared in a manner similar to the procedure for **Iodo-UBD-MA** but using 5-iodoisophthalic acid. The reaction yield was 58%. IR (NaCl, cm^{-1}) 3502, 3346, 2931, 2863, 1689, 1606, 1549, 1482, 1455, 1421, 1351, 1302, 1238, 1201, 1110, 1028. ^{1}H NMR (DMSO-d_6, 500 MHz) δ 8.43 (*s*, 2H), 7.43 (*d*, *J* = 2.0 Hz, 2H), 7.26 (*t*, *J* = 2.0 Hz, 1H), 6.05 (*t*, *J* = 5.5 Hz, 2H), 3.46−3.50 (*m*, 38H), 3.43−3.49 (*m*, 4H), 3.39−3.41 (*m*, 4H), 3.33−3.38 (*m*, 6H), 3.30 (*s*, 6H), 3.02 (*q*, *J* = 6.7 Hz, 4H), 1.47 (*quin*, *J* = 7.0 Hz, 4H), 1.39 (*quin*, *J* = 7.0 Hz, 4H), 1.32−1.25 (*m*, 8H). ^{13}C NMR ($CDCl_3$, 126 MHz) δ 155.90, 141.42, 121.44, 108.29, 94.77, 72.00, 71.34, 70.80, 70.67, 70.65, 70.09, 59.11, 39.90, 29.94, 29.37, 26.54, 25.83. ESI-MS *m*/*z* 561.24 $[M + 2Na]^{2+}$. HRMS (ESI) calculated for $C_{46}H_{85}N_4O_{16}INa_2$ $[M + 2Na]^{2+}$, 561.2395; found, 561.2412.

*1-(4-(1-Oxyl-2,2,6,6-tetramethyl-3,6-dihydro(2H)pyridine-4-yl)phenyl)-3-(2,5,8,11,14,17,20-heptaoxahexacosane-26-yl)urea (**TEMPO-UBD-MA (1)**).* **Iodo-UBD-MA** (320 mg, 0.5 mmol), $Pd(PPh_3)_4$ (28.9 mg, 0.025 mmol), 2,2,6,6-tetramethyl-4-(4,4,5,5-tetramethyl-1,3,2-dioxaborolan-2-yl)-3,6-dihydropyridin-1(2*H*)-yloxyl

DOI: 10.1021/acs.langmuir.7b01126
Langmuir 2017, 33, 7810−7817

radical (168 mg, 0.6 mmol), and degassed 1,4-dioxane (4 mL) were placed in a three-necked flask and bubbled carefully with N_2 gas for 30 min. To this reaction mixture, a 10% Na_2CO_3(aq) solution (10 mL) was added and stirred at 100 °C for 6 h. Brine added to the reaction mixture was extracted with $CHCl_3$ three times, and the combined organic layer was dried over $MgSO_4$ and then evaporated under reduced pressure. The crude residue was chromatographed on silica gel using $CHCl_3$/MeOH (100:1−50:1) as the eluent to obtain an orange oil (197 mg, 0.30 mmol) with a 59% yield. IR (NaCl, cm^{-1}) 3516, 3339, 2929, 2862, 1696, 1668, 1602, 1558, 1453, 1360, 1249, 1201, 1114, 1033, 850. ^{1}H NMR (DMSO-d_6 + ascorbic acid, 500 MHz) δ 8.38 (*s*, 1H), 7.33 (*d*, J = 8.5 Hz, 2H), 7.26 (*d*, J = 8.2 Hz, 2H), 6.07 (*t*, J = 5.8 Hz, 1H), 5.84 (*s*, 1H), 3.50−3.45 (*m*, 26H), 3.23 (*s*, 3H), 3.06 (*q*, J = 6.5 Hz, 2H), 2.37 (*s*, 2H), 1.49 (*quin*, J = 7.0 Hz, 4H), 1.42 (*quin*, J = 7.0 Hz, 4H), 1.34−1.26 (*m*, 4H), 1.21 (*s*, 6H), 1.13 (*s*, 6H). ^{13}C NMR (DMSO-d_6 + ascorbic acid, 126 MHz) δ 155.13, 132.64, 128.88, 128.66, 126.88, 126.66, 126.02, 125.07, 117.34, 71.32, 70.31, 69.83, 69.62, 69.53, 58.09, 29.78, 29.24, 26.28, 25.47. ESI-MS m/z 689.42 $[M + Na]^+$. HRMS (ESI) calculated for $C_{35}H_{60}N_3O_9Na$ $[M + Na]^+$, 689.4222; found, 689.4245.

*1,1′-(5-(1-Oxyl-2,2,6,6-tetramethyl-3,6-dihydro(2H)pyridin-4-yl)-phenyl-1,3-diyl)bis(3-(2,5,8,11,14,17,20-heptaoxahexacosan-26-yl)-urea) (**TEMPO-UBD-DA (2)**).* **Iodo-UBD-DA** (539 mg, 0.5 mmol), $Pd(PPh_3)_4$ (28.9 mg, 0.025 mmol), 2,2,6,6-tetramethyl-4-(4,4,5,5-tetramethyl-1,3,2-dioxaborolan-2-yl)-3,6-dihydropyridin-1(2*H*)-yloxyl radical (168 mg, 0.6 mmol), and degassed 1,4-dioxane (4 mL) were placed in a three-necked flask and carefully bubbled with N_2 gas for 30 min. To this reaction mixture, a 10% Na_2CO_3(aq) solution (10 mL) was added and stirred at 100 °C for 6 h. Brine added to the reaction mixture was extracted with $CHCl_3$ three times, and the combined organic layer was dried over $MgSO_4$ and then evaporated under reduced pressure. The crude residue was chromatographed on silica gel using $CHCl_3$/MeOH (100:1−50:1) as the eluent to obtain an orange oil (211 mg, 0.20 mmol) with a 40% yield. IR (NaCl, cm^{-1}) 3516, 3339, 2929, 2862, 1696, 1668, 1602, 1558, 1453, 1360, 1249, 1201, 1114, 1033, 850. ^{1}H NMR (DMSO-d_6 + ascorbic acid, 500 MHz) δ 8.35 (*s*, 2H), 7.28 (*t*, J = 1.7 Hz, 1H), 7.05 (*d*, J = 1.7 Hz, 2H), 5.99 (*t*, J = 5.5 Hz, 2H), 5.79 (*s*, 1H), 3.52−3.46 (*m*, 36H), 3.40−3.37 (*m*, 16H), 3.23 (*s*, 6H), 3.05 (*q*, J = 6.3 Hz, 4H), 2.33 (*s*, 2H), 1.49 (*quin*, J = 6.5 Hz, 4H), 1.41 (*quin*, J = 6.5 Hz, 4H), 1.33−1.28 (*m*, 8H), 1.22 (*s*, 6H), 1.14 (*s*, 6H). ^{13}C NMR (DMSO-d_6 + ascorbic acid, 126 MHz) δ 172.80, 116.02, 108.32, 105.43, 91.32, 87.91, 84.49, 83.48, 79.24, 78.98, 78.71, 74.81, 73.28, 71.28, 70.28, 69.79, 69.58, 69.49, 58.05, 29.77, 29.21, 26.23, 25.44. ESI-MS m/z 574.34 $[M + 2Na]^{2+}$. HRMS (ESI) calculated for $C_{55}H_{100}N_5O_{17}Na_2$ $[M + 2Na]^{2+}$, 574.3449; found, 574.3459.

Standard Preparation Method of Radical Nanoparticles (RNP). Radicals **1** and **2** were dissolved in saline solutions with sonication in an ice bath for approximately 120 s. The dissolved transparent solutions without further filtration were used as samples for various measurements.

Electron Magnetic Resonance (ESR). ESR spectra were recorded on a Bruker Biospin ESR300 EPR X-band (9.4 GHz) spectrometer equipped with a microwave frequency counter. Sample solutions in saline were placed in capillary tubes and were analyzed at 20−22 °C.

Dynamic Light Scattering (DLS) and Zeta Potential. DLS measurements were performed on a Zetasizer Nano ZS (Malvern Instruments Ltd.). Sample solutions in saline were placed in polystyrol/polystyrene tubes. The zeta potential of the samples was analyzed using the above-described apparatus at 20 °C for **1** and 25 °C for **2**, above and below a critical transition concentration.

Transmission Electron Microscopy (TEM). TEM images were taken on a FEI Tecnai20 machine. The samples (0.5, 1.0, and 5 mM) for TEM measurement were prepared as follows: The corresponding solutions (50 μL) were dropped onto a carbon grid. After approximately 30 s, the residual solution was blotted using KimWipes. To prepare negative stained images, 50 μL of a solution containing 5% uranyl acetate solution was again dropped on the grid, and then the residual solution was blotted using KimWipes. The resulting grids were air dried for 15 min and used as samples.

log *P* Calculation. log *P* values were obtained from the calculation methods. The modeling studies were performed using MacroModel ver. 11.2 as implemented in Maestro ver. 10.5. The structures of **1′** and **2′** (with the nitroxyl radical in TEMDO replaced by a carbonyl group) were optimized in molecular mechanics with the OPLS3 force field with a dielectric constant of 1.0. The convergence criterion was set to an energy gradient of 0.05 kJ/mol. Conformational searches were then performed using the Monte Carlo molecular modeling (MCMM) method to generate 1000 structures, which were individually minimized into local minima. The most stable conformations of **1′** and **2′** were subsequently optimized at the DFT (B97-D/3-21G*) level using the D.01 revision of the Gaussian 09 program package.[21,22] Their corresponding nitroxyl radicals **1** and **2** were also optimized at the same level of theory (Figure S6). Frequencies were analytically computed at the B97-D/6-31G* level of theory to give gas-phase Gibbs free energies (298 K, 1 atm) and to confirm whether the structures are minima (no imaginary frequencies) or transition states (only one imaginary frequency).

log *P* was estimated from the computed free transfer energy according to equation[23]

$$\log P = \frac{(\Delta G_{\mathrm{sol}(n\text{-octanol})} - \Delta G_{\mathrm{sol}(\mathrm{water})})}{2.30RT}$$

where R is the gas constant and T is the temperature.

To estimate log *P* (*n*-octanol/water) values, gas-phase DFT-optimized conformers (**1′**, **2′**, **1**, and **2**) were reoptimized in *n*-octanol and water, respectively ((U)B97-D/6-31G*//(U)B97-D/3-21G*:SMD = *n*-octanol or water) . The results of each optimization were used to evaluate the free-energy difference for the two solvents. Calculated log *P* values were 5.03 for **1′**, 2.85 for **2′**, 5.05 for **1**, and 3.86 for **2** (Table S1).

T_1- and T_2-Weighted MRI and Relaxivity of the Samples. MRI acquisitions of CAs were performed on a 1.0 T-MRI scanner (BrukerBiospin, Ettlingen, Germany) with a solenoid coil (35 mm inner diameter, transmission, and reception, Aspect Imaging, Shoham, Israel). An aqueous solution of the contrast agents was initially put into a polymerization chain reaction (PCR) tube cluster plate, and the PCR tube cluster plate was set in the center of the volume coil. The sample temperature was maintained at 23.0 ± 0.5 °C throughout all of the experiments by using an air condition. Using the MRI scanner, horizontal single-slice T_1-weighted MR images were acquired with the following parameters: spin echo, TR/TE = 400/10 ms, slice thickness = 2.0 mm, matrix = 256 × 256, field of view (FOV) = 38.4 × 38.4 mm^2, number of averages (NA) = 1, and number of slices = 1. For longitudinal relaxation time (T_1) and longitudinal relaxivity (r_1) calculations, horizontal single-slice inversion−recovery MRI was performed using RARE (rapid acquisition with relaxation enhancement) acquisition with the following parameters: TR = 10 000 ms, TE = 20 ms, inversion time = 52, 100, 200, 400, 800, 1600, 3200, 6400 ms, matrix size = 128 × 128, FOV = 38.4 × 38.4 mm^2, slice thickness = 2.0 mm, RARE factor = 4, and NA = 1. For transverse relaxation time (T_2) and longitudinal relaxivity (r_2) calculations, spin-echo mulch slice mulch echo sequence was used with the following parameters: TR = 20000 ms, TE = 20 ms (256 echoes, for contrast agent measurement) or 40 ms (256 echoes, for saline measurement), matrix size = 64 × 64, FOV = 38.4 × 38.4 mm^2, slice thickness = 2.0 mm, and NA = 1.

In Vivo Examination Using Mice. *BALB/c* nude mice bearing colon-26 tumors on the lower back were used to test the compatibility of the MRI CAs. After intravenous administration of **2** (100 mM, 100 μL) and 4-hydroxy-2,2,6,6-tetramethylpiperidin-1-oxyl (TEMPOL) (300 mM, 200 μL) saline solutions, the intensities of the T_1-weighted images in the tumor and the muscle tissue (regions of interest, ROIs) were noted every 20 s during a period of 30 min using a 7.0 T-MRI scanner (BrukerBiospin, Ettlingen, Germany) equipped with a volume coil (35 mm inner diameter, transmission and reception, Rapid Biomedical, Rimpar, Germany).

DOI: 10.1021/acs.langmuir.7b01126
Langmuir 2017, 33, 7810−7817

RESULTS AND DISCUSSION

Syntheses. **TEMDO-UBD** analogues **1** and **2** were prepared in a manner similar to that for **TEMDO-UBD-1** (Scheme S1).[14] According to the Suzuki-Miyaura coupling reaction,[17,18] corresponding iodo-benzene derivatives having one or two amphiphilic side chains were reacted with tetramethyl-4-(4,4,5,5-tetramethyl-1,3,2-dioxaborolan-2-yl)-3,6-dihydropyridin-1(2*H*)-yloxyl radical (boron-TEMDO) in the presence of a palladium catalyst (Scheme S1) to obtain crude **1** and **2** as reddish oils. The crude products were chromatographed on silica gel using $CHCl_3$/MeOH as the eluent and produced reddish oils with 59 and 40% yields for **1** and **2**, respectively.

Self-Assembly Behavior. The self-assembly behavior of **1** and **2** was evaluated using ESR, DLS, and TEM and interpreted in terms of the change in the corresponding ESR spectra, the hydrodynamic diameter (D_H) observed by DLS, and the images recorded by TEM.

In the ESR spectra, three well-resolved signals due to the splitting of the nitrogen nuclear spin were observed (Figure 2a). With increasing concentration, the signals of both **1** and **2** became slightly broadened. From the signal width and the intensity in each spectrum, the τ_R values were estimated according to Kivelson's equation (eq 1),[19,20] where h_{+1}, h_0, and h_{-1} denote the peak intensities in the lowest, the middle, and the highest fields, respectively, and ΔH_0 indicates the peak width of the middle peak. The given τ_R values at the lowest (~50 μM) concentration of **1** and **2** were 0.8×10^{-10} and 1.5×10^{-10} s, respectively. At a solution concentration of 1 mM, the τ_R values grew to 1.1×10^{-10} and 1.8×10^{-10} s for **1** and **2**, respectively, suggesting that sized-up behavior due to self-assembly takes place. The τ_R values of **1** and **2** were plotted as a function of the sample concentration (Figure 1b); a discrete change in τ_R was noticed at 150 and 250 μM for **1** and **2**, respectively. The concentrations at which the discontinuity occurs depict the critical transition concentrations (CTCs) such as the CAC and any other transformations within the NPs. Therefore, the resulting CTC_1 for **1** and CTC_2 for **2** are the concentrations at which either the RNPs begin forming or other transformations take place or a combination of both.

$$\tau_R = 6.6 \times 10^{-10} \times \{\sqrt{(h_0/h_{+1})} + \sqrt{(h_0/h_{-1})} - 2\} \times \Delta H_0 \quad (1)$$

To reveal the particle sizes of **1** and **2** in solution, the D_H values were analyzed below and above $CTC_{1\ or\ 2}$ by DLS (Figure 3a). At the same time, the zeta potential values were recorded. In 0.05 mM **1**, the peak corresponding to the D_H appeared at around 50 nm, indicating the formation of **RNP 1**. On varying the concentration from 0.05 to 3 mM involving CTC_1, the D_H size gradually increased from 50 to 90 nm (Figure 3a-1,a-3). In **2** solution, above CTC_2, a D_H of 30−100 nm was observed along with polydispersity, indicating the formation of **RNP 2** (Figure 3a-2). In contrast, the solution below CTC_2 gave rise to no detectable peaks that corresponded to NPs; this is due to the low magnitude of the scattered light. These results indicate that the size transformation of **RNP 1** takes place at CTC_1 and the transformation of the monomer into **RNP 2** takes place at CTC_2, and thus CTC_2 equals CAC (vide supra). Interestingly, regarding the concentration dependence of the zeta potential, **1** exhibited a change in the ζ value during the transformation, −9 and −4 mV below and above CTC_1, respectively, accompanied by the discontinuous change (Figure 3a-3). The resulting curvature with the discontinuous points around 150 μM was detected by the change in τ_R (Figure 2b). In the case of **2**, no concentration dependence was noticed (Table 1). In TEM images above $CTC_{1\ or\ 2}$, spherical RNPs of 10−100 nm in size were detected (Figure 3b). The sizes of the observed RNPs were measured to create histograms that analyze the size distribution as a function of the particle size, and the particle sizes of **RNP 1** and **2** were found to be 10−30 and 10−60 nm, respectively. The corresponding sizes calculated from TEM images were slightly smaller than those of D_H in DLS, suggesting that the RNPs swell in solution. No remarkable concentration dependence was seen in the TEM-calculated particle sizes above $CTC_{1\ or\ 2}$, but an attempt to detect the size of **RNP 2** below CTC_2 failed owing to the low concentration. DLS results, TEM images, and the size distributions in TEM are shown in Figure 3, accompanied by the concentration dependence of D_H and ζ of **RNP 1**. The resulting values of τ_R

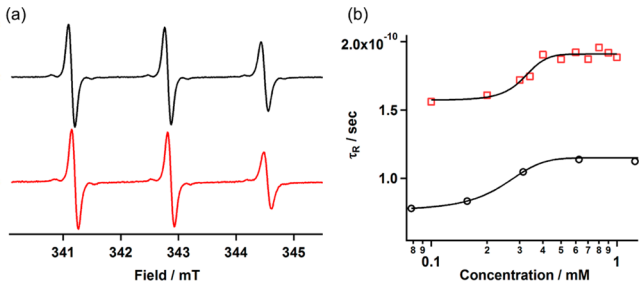

Figure 2. (a) Normalized ESR spectra of 1 mM saline solutions of **1** (black) and **2** (red). (b) Plots of τ_R values vs concentration of **1** (black) and **2** (red).

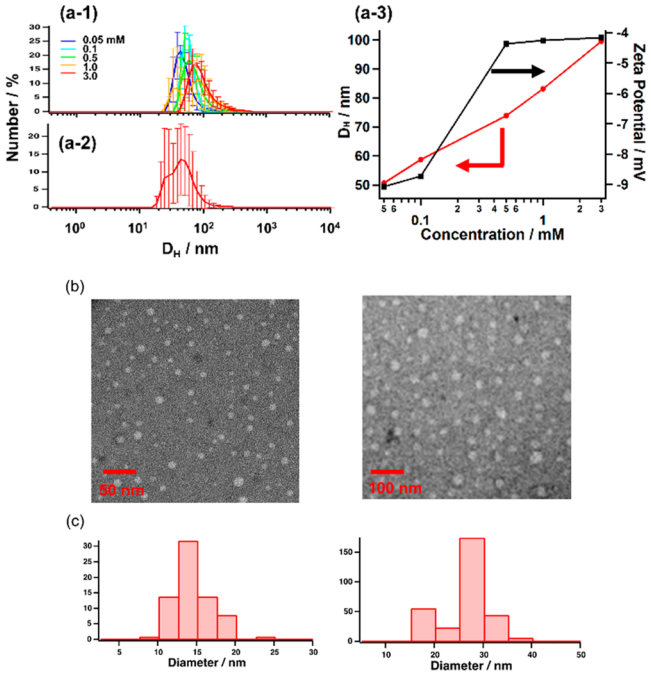

Figure 3. D_H distributions of **RNP 1** (a-1) and **2** (a-2) in saline. (a-3) Change in D_H and ζ values with the concentration dependence of **RNP 1**. Each arrow corresponds to the related axis. (b) TEM images in pure water solutions. (c) Size distributions of RNPs are shown in panels (b). The results of **1** and **2** are shown in the left and right panels, respectively.

DOI: 10.1021/acs.langmuir.7b01126
Langmuir 2017, 33, 7810−7817

Table 1. Values of τ_R, Size, and Zeta Potential (ζ) for RNP 1 and 2 and TEMPO-UBD 1 and 2 at Room Temperature

	$\tau_R/10^{-10}$s		size/nm		
			D_H (ζ/mV)[b]		TEM[c]
	below CTC	above CTC	below CTC	above CTC	above CTC
RNP 1[a]	0.8	1.1	50−60 (−8.7 to −9.0)	70−90 (−4.2)	10−30
RNP 2[a]	1.5	1.8	[d]	30−100(−6.6)	10−60
TEMDO-UBD[e]	1.77−2.05	2.04−2.34	10−150		10−150
TEMPO-UBD[f]			2.8		10−500

[a]CTC_1 of **1** and CTC_2 of **2** correspond to 150 and 250 μM solutions, respectively. See the main text. [b]50 μM and 5 mM saline solutions as below and above $CTC_{1\ or\ 2}$ for **1** and **2**. [c]1 and 5 mM pure water solutions of **1** and **2**. [d]Not determined. [e]Reference 13. CTC was determined to be CAC at 0.66−0.77 mM. [f]Reference 14. CTC was undetermined.

and ζ and the sizes for **RNP 1** and **2** are summarized in Table 1. Furthermore, photographs of Tyndall scattering of the **RNPs** are shown in Figure S5.

The self-assembly behavior of **TEMDO UBD** derivatives to form **RNP 1** and **2** is illustrated in Figure 4. Despite being

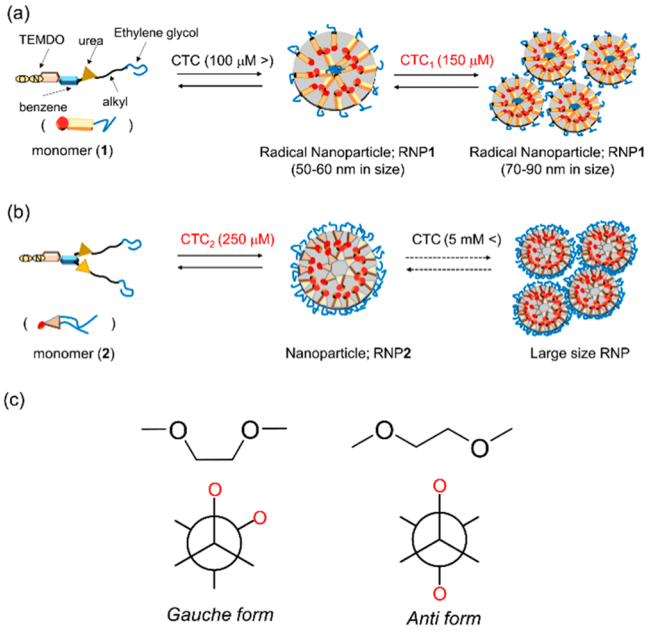

Figure 4. Illustration of the plausible formations of **RNP 1** (a) and **2** (b) together with individual CTC values. (c) Plausible conformations of the ethylene glycol unit with gauche (cis) and anti (trans) forms illustrated by a Newman projection.

below CTC_1, **1** having one OEG formed 50−60 nm **RNP 1** as a result of the numerous intermolecular interactions in the UBD framework (hydrogen bonds, $\pi-\pi$ stacking, and hydrophilic interactions). Above CTC_1, the resulting **RNP 1** exhibited further self-assembly behavior, giving rise to a size-up RNP (**RNP 1(L)**), 70−100 nm in size. In contrast, **2**, which has two OEG units that form RNP above CTC_2 (CAC), indicates an equilibrium reaction between monomer **2** and **RNP 2**. Compared to **1**, which has one OEG, **2** may exhibit a higher CAC as a result of its enhanced water-soluble property. The log *P* values of **1** and **2** were calculated by DFT[21−23] and were found to be 5.05 and 3.86 for **1** and **2**, respectively. These results indicate that **1** possesses a stronger hydrophobic property than **2** and easily forms the RNPs (Figure S6 and Table S1). In addition, the observed changes in the zeta potential of **1** upon varying the concentration may be related to the conformational changes of the ethylene glycol in OEG (Figure 4c). In a solution below CTC_1, because the ethylene glycol is highly polar, a gauche (cis) form corresponding to the oxygen atoms in the ethylene glycol is dominant (Figure 4c left).[24,25] As a result, the zeta potential shows a larger negative value (−9 mV). In contrast, when the solution is above CTC_1, **RNP 1** undergoes further self-assembly with hydrophobic interactions, resulting in conformational changes in the ethylene glycol. Because the ethylene glycols prefer a lower polarity, an anti (trans) form corresponding to the oxygen atoms is dominant (Figure 4c right). As a consequence, the zeta potential has a smaller negative value (−4 mV).[26] Plausible equilibrium reactions between the monomers and RNPs to form self-assembled RNPs are illustrated in Figure 4a,b. Plausible conformations of an ethylene glycol unit with gauche (cis) and anti (trans) forms are illustrated by a Newman projection and are shown in Figure 4c.

T_1- and T_2-Weighted Images and Relaxivity Values (r_1 and r_2) of the NPs. T_1- and T_2-weighted images were taken to estimate the T_1 and T_2 relaxation times attributed to the water proton (1 T at 23 °C). Because spherical **RNPs 1** and **2** contain the stable radical units of TEMDO, the T_1 and T_2 relaxation times are shortened by the paramagnetic relaxation enhancement (PRE) effect.[27,28] In addition, large molecules assist in further shortening the T_1 and T_2 relaxation times. The compatibilities of the MRI CAs are evaluated as relaxivity values, r_1 and r_2, which were calculated using eqs 2 and 3, where T_0 and C denote the corresponding T_1 and T_2 relaxation times without CAs and concentration, respectively.

$$1/T_1 = 1/T_0 + r_1C \quad (2)$$

$$1/T_2 = 1/T_0 + r_2C \quad (3)$$

Figure 5 shows the T_1-weighted images of **1** and **2** in the concentration range of 5−0.078 mM in saline solutions. At 5 mM concentration, when the T_1-weighted images of **1** and **2** are compared, the image corresponding to **2** was clearly brighter than that of **1**, indicating that **2** has a longer T_1 relaxation time than **1**. At lower concentrations below 1 mM, the T_1-weighted images of **1** and **2** exhibited a similar brightness to each other, indicating that the abilities at lower concentration are similar to each other. T_1- and T_2-weighted images of **1** and **2** at different concentrations are shown in Figures 5 and S7.

To confirm the ability of **1** and **2** to act as MRI CAs, the resulting relaxation times were inverted to T_1^{-1} and T_2^{-1}, and their values were plotted as a function of concentration (Figure 6) to obtain r_1 and r_2 values in the slope. In the lower concentration range of 0.078−1.25 mM, the r_1 values corresponding to **RNP 1** and **2** were 0.29 and 0.12 mM^{-1} s^{-1}; in addition, the related r_2 of **RNP 1** was 0.26 mM^{-1} s^{-1}, but

DOI: 10.1021/acs.langmuir.7b01126
Langmuir 2017, 33, 7810−7817

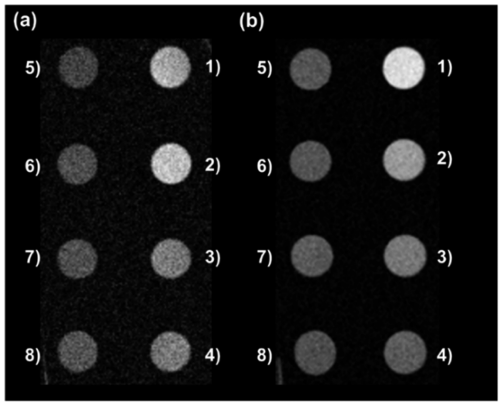

Figure 5. T_1-weighted images of **1** (a) and **2** (b). Numerical notations along the images indicate that the saline solutions containing CAs corresponded to concentrations of 5 (1), 2.5 (2), 1.25 (3), 0.625 (4), 0.312 (5), 0.156 (6), and 0.078 mM CA (7) and no CA (8).

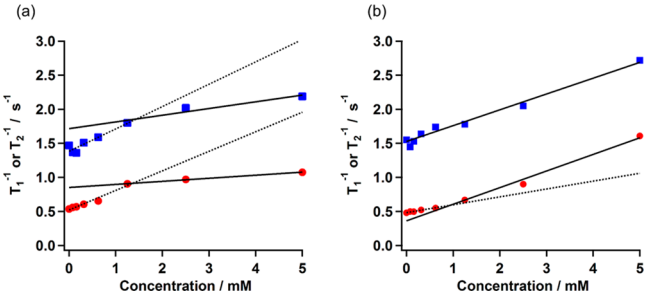

Figure 6. Plots of T_1^{-1} and T_2^{-1} as a function of the concentrations of **1** (a) and **2** (b). Red circles and blue squares indicate the inversion of T_1 and T_2 relaxation times, respectively. Solid and dotted lines indicate the fitting lines at the corresponding higher and lower concentrations.

values of **RNP 2** were disordered in the range to afford a nonsuperimposed fitting line. These values are similar to those of the TEMPO radical of low molecular weight (r_1 and r_2 were 0.18 and 0.21 mM^{-1} s^{-1}, respectively). Interestingly, in the highly concentrated solutions (concentrations above 1.25 mM), that is, the solution above $CTC_{1\ or\ 2}$, the r_1 and r_2 values are were different. **RNP 1(L)** had r_1 and r_2 values of 0.05 and 0.10 mM^{-1} s^{-1}, respectively, whereas **RNP 2** had r_1 and r_2 values of 0.24 and 0.26 mM^{-1} s^{-1}, respectively, indicating that the corresponding relaxivity values of **RNP 2** are much larger than those of **RNP 1(L)**. Plots of T_1^{-1} and T_2^{-1} as a function of the concentrations of **1** and **2** are shown in Figure 6. The relaxivity values are summarized in Table 2.

Generally, RNPs possessing a large molecular size can induce an enhanced T_1-weighted image, eventually giving rise to high relaxivity values due to the PRE effect, in addition to suppressing the fast motion of the paramagnetic species (vide supra). In the case of **RNP 1(L)**, despite the particles being 70–90 nm in size and accompanied by an increasing τ_R value (Table 1), the highly concentrated solution gave rise to a smaller relaxivity value. This discrepancy can be explained as a byproduct of dehydration within the RNPs around spin sources; when the number of water molecules is reduced, the relaxivity values are small (frequent interactions between water molecules and spin sources can lead to increased relaxivity values[27,28] and even large τ_R values). In some **UBDs**, the dehydration process is characterized by a lower critical solution temperature (LCST). In fact, the concentration above 0.5 mM for **1** and **2** exhibited dehydration behavior at LCSTs, accompanied by a remarkable concentration dependence (Figure S8). In addition, for the r_1 and r_2 values in the range of 0.078–5.0 mM at 29 °C, which is above the LCST (>∼500 μM), the relaxivity values were similar to those at 23 °C above 1.25 mM (Table 2). Eventually, in the solution above CTC_1, **RNP 1** shows further self-assembly due to the strong hydrophobic interactions and the dehydration process, producing **RNP 1(L)** with a small relaxivity value. **RNP 1** contains more water molecules than **RNP 1(L)**. In the **2** solution above CTC_2, typical self-assembly behavior takes place via the multiple intermolecular interactions in the hydration process (not dehydration), producing **RNP 2** having a high relaxivity value as well as **RNP 1**. The discrepancy in the inflection points obtained from ESR (150 μM) and the r_1 value (1.5 mM) for **RNP 1** might originate from the different degrees of the dehydration processes. Namely, in the concentration above CTC_1, the concentration dependence of the number of water molecules close to the NO spin might be present within **RNP 1(L)**. The plausible self-assembly of **RNP 1** and **2** by the dehydration and hydration processes is illustrated in Figure 7.

Table 2. Relaxivity Values Estimated from the Related Relaxation Times of RNP 1 and 2[a]

	RNP 1/mM		RNP 2/mM	
relaxivity/mM^{-1} s^{-1}	0.078–1.25	1.25–5	0.078–1.25	1.25–5
r_1	0.287	0.047	0.116	0.244
	0.064[b]			
r_2	0.261	0.099	[c]	0.256
	0.086[b]			

[a]Acquisition under 1 T at 23 °C. [b]Acquisition at 29 °C. [c]It is estimated that r_2 has R^2 = 0.704.

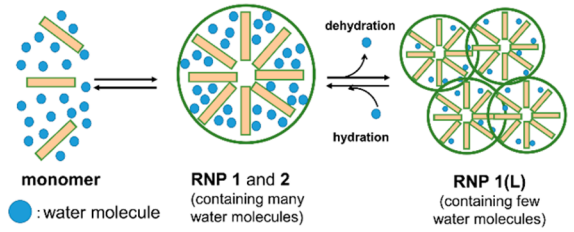

Figure 7. Illustration of the formation of RNPs by the dehydration and hydration processes.

In Vivo Examination Using Mice. To confirm the compatibility of the developed RNPs for MR bioimaging, in vivo examinations using **RNP 2** were performed, and the signal intensities of the T_1-weighted images in ROIs were monitored (Figures 8 and S10). 4-Hydroxy-2,2,6,6-tetramethylpiperidin-1-oxyl (TEMPOL) was used as the reference compound. Immediately after an intravenous administration of **RNP 2** or TEMPOL, the signal intensities corresponding to the ROI showed a subtle enhancement and then underwent rapid attenuation. The attenuation behaviors in the tumor tissue were fitted with a function of linear expression (eq 4) to yield the rate constant k_{obs} values of 9.5×10^{-3} and 3.2×10^{-2} s^{-1} in **RNP 2** and TEMPOL, respectively (Figure 8d). These results indicate that the attenuation of **RNP 2** is slower than that of TEMPOL. Similarly, the rate constant k_{obs} in muscle tissues exhibited values of 7.3×10^{-3} and 9.5×10^{-3} s^{-1} for **RNP 2** and TEMPOL, respectively (Figure S11). However, these rapid

DOI: 10.1021/acs.langmuir.7b01126
Langmuir 2017, 33, 7810–7817

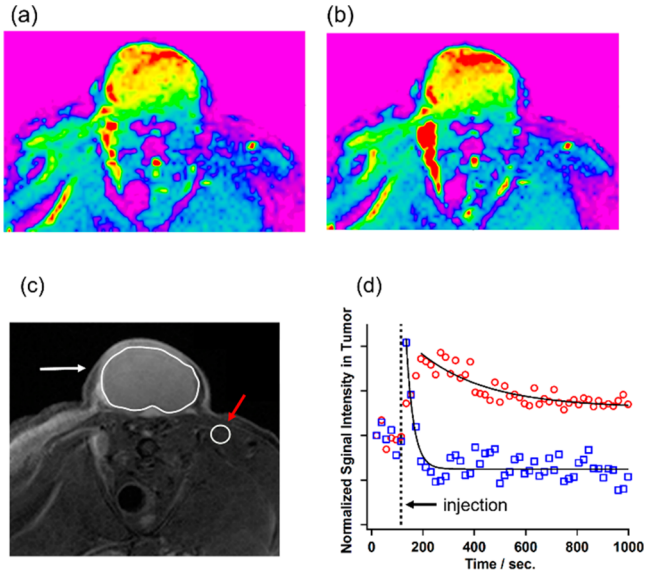

Figure 8. T_1-weighted images around a tumor tissue before (a) and after (b) an intravenous administration of **RNP 2** (100 mM, 100 μL). (c) T_2-weighted image around a tumor tissue. White and red arrows indicate that the tumor and muscle tissue collected the signal intensity in T_1-weighted images. (d) Time dependence of the normalized signal intensities in the tumor tissues after the intravenous administration of **RNP 2** (red circles) and TEMPOL (blue squares). Solid black lines indicate the fitting of results per the linear expression.

attenuations (k_{obs} on the order of 10^{-2}–10^{-3} s) indicate that side reactions due to bioreduction by materials such as ascorbic acid occur in addition to metabolism.

$$\text{signal intensity} = \exp(-k_{obs} \times \text{time}) \quad (4)$$

CONCLUSIONS

We analyzed the self-assembly behavior of **1** and **2** consisting of the UBD framework with a stable radical. Resulting **RNPs 1** and **2** were evaluated for their abilities as MRI CAs. **1** and **2** formed spherical **RNPs** even at low concentrations (e.g., below CTC_1 for **RNP 1** and above CTC_2 for **RNP 2**), unlike the **TEMPO-UBDs** reported previously.[13,14] In the case of **RNP 1**, the additional self-assembly behavior of the **RNPs** with CTC_1 took place in highly concentrated solutions and was accompanied by a dehydration process. The r_1 values above $CTC_{1\ or\ 2}$ in **RNP 1** or **2** were distinct; the r_1 value of **RNP 2** was 5 times larger than that of **RNP 1**. Such distinct r_1 values may be due to differences in the number of water molecules surrounded by the radical moiety; e.g., **RNP 1** and **2** possess many water molecules, but **RNP 1(L)** possesses few water molecules. These results indicate that **RNP 1** and **2**, at low concentrations, can potentially be used as CAs. In vivo examination using **RNP 2** that has high relaxivity values produced a slightly enhanced T_1-weighted image signal that undergoes rapid attenuation in the tumor tissues. Furthermore, the signal intensity of **RNP 2** showed a slower attenuation compared to that of TEMPOL. These results suggest that the self-assembled **RNP 2** having a larger molecular size allows us to extend the time period for attenuation in the signal intensity as a result of the protection from bioreduction materials. To further extend the attenuation time of the signal, a study of RNPs containing tetraethyl groups, with resistance against bioreductants,[29,30] is currently underway in our group. In addition, we are studying RNPs to develop dual imaging systems using MRI and emission[31] properties.

ASSOCIATED CONTENT

Supporting Information

The Supporting Information is available free of charge on the ACS Publications website at DOI: 10.1021/acs.langmuir.7b01126.

Synthesis route, Tyndall effect, DFT calculation of log *P*, T_2-weighted images, LCST behavior of **1** and **2**, in vivo t_1-weighted images using the TEMPOL radical, signal intensity changes in muscle tissues using **2** and TEMPOL, copies of ^{1}H NMR and ^{13}C NMR related to new compounds, and Cartesian coordinates of the optimized structures (PDF)

AUTHOR INFORMATION

Corresponding Author

*E-mail: karasawa@ac.shoyaku.ac.jp.

ORCID

Satoru Karasawa: 0000-0002-3107-442X

Notes

The authors declare no competing financial interest.

ACKNOWLEDGMENTS

The authors thank Dr. Noboru Koga for helpful discussions and Dr. Sayaka Shibata and Nobuhiro Nitta for assistance with the animal experiments. This work was partially supported by the PRESTO Program on Molecular Technology from the Japan Science Technology Agency (JST). Optical imaging and in vivo studies were also financially supported by the Center of Innovation Program (COI) stream of the JST and by a Jisedai Grant/Innovative Cancer Grant from the Japan Agency for Medical Research and Development.

REFERENCES

(1) Monti, M.; Brandt, L.; Ikomi-Kumm, J.; Olsson, H. Microcalorimetric investigation of cell metabolism in tumor cells from patients with non-Hodgkin lymphoma (NHL). *Scand. J. Haematol.* **1986**, *36*, 353–367.

(2) Okabe, K.; Inada, N.; Gota, C.; Harada, Y.; Funatsu, T.; Uchiyama, S. Intracellular temperature mapping with a fluorescent polymeric thermometer and fluorescence lifetime imaging microscopy. *Nat. Commun.* **2012**, *3*, 705.

(3) Nagano, S.; Perentes, J. Y.; Jain, R. K.; Boucher, Y. Cancer cell death enhances the penetration and efficacy of oncolytic herpes simplex virus in tumors. *Cancer Res.* **2008**, *68*, 3795–3802.

(4) Nakanishi, T.; Fukushima, S.; Okamoto, K.; Suzuki, M.; Matsumoto, Y.; Yokoyama, M.; Okano, T.; Sakurai, Y.; Kataoka, K. Development of the polymer micelle carrier system for doxorubicin. *J. Controlled Release* **2001**, *74*, 295–302.

(5) Fang, J.; Nakamura, H.; Maeda, H. The EPR effect: Unique features of tumor blood vessels for drug delivery, factors involved, and limitations and augmentation of the effect. *Adv. Drug Delivery Rev.* **2011**, *63*, 136–151.

(6) Mi, P.; Kokuryo, D.; Cabral, H.; Kumagai, M.; Nomoto, T.; Aoki, I.; Terada, Y.; Kishimura, A.; Nishiyama, N.; Kataoka, K. Hydrothermally synthesized PEGylated calcium phosphate nanoparticles incorporating Gd-DTPA for contrast enhanced MRI diagnosis of solid tumors. *J. Controlled Release* **2014**, *174*, 63–71.

(7) Caravan, P.; Ellison, J. J.; McMury, T. J.; Lauffer, R. B. Gadolinium(III) chelates as MRI contrast agents: Structure, dynamics, and applications. *Chem. Rev.* **1999**, *99*, 2293–2352.

DOI: 10.1021/acs.langmuir.7b01126
Langmuir 2017, 33, 7810–7817

(8) Della Rocca, J.; Liu, D.; Lin, W. Nanoscale Metal-Organic Frameworks for Biomedical Imaging and Drug Delivery. *Acc. Chem. Res.* **2011**, *44*, 957−968.
(9) Kanda, T.; Ishii, K.; Kawaguchi, H.; Kitajima, K.; Takenaka, D. High Signal Intensity in the Dentate Nucleus and Globus Pallidus on Unenhanced T1-weighted MR Images: Relationship with Increasing Cumulative Dose of a Gadolinium-based Contrast Material. *Radiology* **2014**, *270*, 834−841.
(10) Frenzel, T.; Lengsfeld, P.; Schirmer, H.; Hütter, J.; Weinmann, H. J. Stability of Gadolinium-Based Magnetic Resonance Imaging Contrast Agents in Human Serum at 37 degrees C. *Invest. Radiol.* **2008**, *43*, 817−s828.
(11) Rajca, A.; Wang, Y.; Boska, M.; Paletta, J. T.; Olankitwanit, A.; Swanson, M. A.; Mitchell, D. G.; Eaton, S. S.; Eaton, G. R.; Rajca, S. Organic Radical Contrast Agents for Magnetic Resonance Imaging. *J. Am. Chem. Soc.* **2012**, *134*, 15724−15727.
(12) Hayashi, H.; Karasawa, S.; Tanala, A.; Odoi, K.; Chikama, K.; Kuribayashi, H.; Koga, N. Water-proton relaxivity of hyperbranched polymers carrying TEMPO radicals. *Magn. Reson. Chem.* **2009**, *47*, 201−204.
(13) Hayashi, H.; Ohkubo, K.; Karasawa, S.; Koga, N. Assemblies of Functional Small-Sized Molecules Having 4-Amino-2,2,6,6-tetramethylpiperidine-1-oxyl Responsive to Heat and pH in Water and Their Water Proton Relaxivities. *Langmuir* **2011**, *27*, 12709−12719.
(14) Morishita, K.; Murayama, S.; Araki, T.; Aoki, I.; Karasawa, S. Thermal- and pH-Dependent Size Variable Radical Nanoparticles and Its Water Proton Relaxivity for Metal-Free MRI Functional Contrast Agents. *J. Org. Chem.* **2016**, *81*, 8351−8362.
(15) Tanimoto, E.; Karasawa, S.; Ueki, S.; Nitta, N.; Aoki, I.; Koga, N. Unexpectedly large water-proton relaxivity of TEMPO incorporated into micelle-oligonucleotides. *RSC Adv.* **2013**, *3*, 3531−3534.
(16) Sato, Y.; Hayashi, H.; Okazaki, M.; Aso, M.; Karasawa, S.; Ueki, S.; Suemune, H.; Koga, N. Water-proton relaxivities of DNA oligomers carrying TEMPO radicals. *Magn. Reson. Chem.* **2008**, *46*, 1055−1058.
(17) Raders, S. M.; Moore, J. N.; Parks, J. K.; Miller, A. D.; Leißing, T. M.; Kelley, S. P.; Rogers, R. D.; Shaughnessy, K. H. Trineopentylphosphine: A Conformationally Flexible Ligand for the Coupling of Sterically Demanding Substrates in the Buchwald-Hartwig Amination and Suzuki-Miyaura Reaction. *J. Org. Chem.* **2013**, *78*, 4649−4664.
(18) Iwanaga, T.; Ogawa, M.; Yamauchi, T.; Toyota, S. Intramolecular Charge-Transfer Interaction of Donor-Acceptor-Donor Arrays Based on Anthracene Bisimide. *J. Org. Chem.* **2016**, *81*, 4076−4080.
(19) Kivelson, D. Electric-Field Fluctuations and Spin Relaxation In Liquids. *J. Chem. Phys.* **1966**, *45*, 1324.
(20) Kundu, K.; Das, R. Saturation recovery electron spin-lattice relaxation studies on benzene anion radical and its derivatives: application of Kivelson-Orbach mechanism of electron spin relaxation. *Mol. Phys.* **2014**, *112*, 1577−1588.
(21) Frisch, M. J.; Trucks, G. W.; Schlegel, H. B.; Scuseria, G. E.; Robb, M. A.; Cheeseman, J. R.; Scalmani, G.; Barone, V.; Mennucci, B.; Petersson, G. A.; Nakatsuji, H.; Caricato, M.; Li, X.; Hratchian, H. P.; Izmaylov, A. F.; Bloino, J.; Zheng, G.; Sonnenberg, J. L.; Hada, M.; Ehara, M.; Toyota, K.; Fukuda, R.; Hasegawa, J.; Ishida, M.; Nakajima, T.; Honda, Y.; Kitao, O.; Nakai, H.; Vreven, T.; Montgomery, J. A., Jr.; Peralta, J. E.; Ogliaro, F.; Bearpark, M.; Heyd, J. J.; Brothers, E.; Kudin, K. N.; Staroverov, V. N.; Kobayashi, R.; Normand, J.; Raghavachari, K.; Rendell, A.; Burant, J. C.; Iyengar, S. S.; Tomasi, J.; Cossi, M.; Rega, N.; Millam, M. J.; Klene, M.; Knox, J. E.; Cross, J. B.; Bakken, V.; Adamo, C.; Jaramillo, J.; Gomperts, R.; Stratmann, R. E.; Yazyev, O.; Austin, A. J.; Cammi, R.; Pomelli, C.; Ochterski, J. W.; Martin, R. L.; Morokuma, K.; Zakrzewski, V. G.; Voth, G. A.; Salvador, P.; Dannenberg, J. J.; Dapprich, S.; Daniels, A. D.; Farkas, Ö.; Foresman, J. B.; Ortiz, J. V.; Cioslowski, J.; Fox, D. J. *Gaussian 09*, Revision D.01; Gaussian, Inc.: Wallingford, CT, 2009.
(22) Calculations were performed with the Gaussian 09 program on a TATARA system at Kyushu University.
(23) Bayat, Z.; Movaffagh. Evaluation of the 1-octanol/water partition coefficient of nucleoside analogs via free energy estimated in quantum chemical calculations. *Russian Journal of Physical Chemistry A* **2010**, *84*, 2293−2299.
(24) Aroua, S.; Tiu, E. G. V.; Ishikawa, T.; Yamakoshi, Y. *Helv. Chim. Acta* **2016**, *99*, 805−813.
(25) Linse, P.; Björling, M. *Macromolecules* **1991**, *24*, 6700−6711.
(26) Mandal, A.; Meda, V.; Zhang, W. J.; Farhan, K. M.; Gnanamani, A. Synthesis, characterization and comparison of antimicrobial activity of PEG/TritonX-100 capped silver nanoparticles on collagen scaffold. *Colloids Surf., B* **2012**, *90*, 191−196.
(27) Sigg, S. J.; Santini, F.; Najer, A.; Richard, P. U.; Meijer, W. P.; Palivan, C. G. Nanoparticle-based highly sensitive MRI contrast agents with enhanced relaxivity in reductive milieu. *Chem. Commun.* **2016**, *52*, 9937−9940.
(28) Ye, D.-X.; Ma, Y.-Y.; Zhao, W.; Cao, H.-M.; Kong, J.-L.; Xiong, H.-M.; Möhwald, H. ZnO-Based Nanoplatforms for Labeling and Treatment of Mouse Tumors without Detectable Toxic Side Effects. *ACS Nano* **2016**, *10*, 4294−4300.
(29) Eggersdorfer, M.; Laudert, D.; Létinolis, U.; McClymont, T.; Medlock, J.; Netschere, T.; Bonrath, W. One Hundred Years of Vitamins-A Success Story of the Natural Sciences. *Angew. Chem., Int. Ed.* **2012**, *51*, 12960−12990.
(30) Braun, L.; Puskas, F.; Csala, M.; Meszaros, G.; Mandl, J.; Banhegyi, G. Ascorbate as a substrate for glycolysis or gluconeogenesis: Evidence for an interorgan ascorbate cycle. *Free Radical Biol. Med.* **1997**, *23*, 804−808.
(31) Araki, T.; Murayama, S.; Usui, K.; Shimada, T.; Aoki, I.; Karasawa, S. Self-Assembly Behavior of Emissive Urea Benzene Derivatives Enables Heat-Induced Accumulation in Tumor Tissue. *Nano Lett.* **2017**, *17*, 2397−2403.

DOI: 10.1021/acs.langmuir.7b01126
Langmuir 2017, 33, 7810−7817